

Full Length Article

Deposition temperature influence on the wear behaviour of carbon-based coatings deposited on hardened steel



D. Feldiorean^{a,b}, D. Cristea^a, M. Tiorean^a, C. Croitoru^a, C. Gabor^{a,*}, L. Jakab-Farkas^c, L. Cunha^d, N.P. Barradas^e, E. Alves^f, V. Craciun^h, A. Marinⁱ, C. Moura^d, J. Lemeⁱ, M. Socol^g, D. Craciun^h, M. Cosnita^k, D. Munteanu^a

^a Transilvania University of Brasov, Materials Science and Engineering Faculty, 29 Eroilor Blvd., 500036 Brasov, Romania

^b Durkopp Adler Romania, Romania

^c Sapientia University, Faculty of Engineering, 540485 Tg. Mures, Romania

^d Centro de Física, Universidade do Minho, Campus de Gualtar, 4710-057 Braga, Portugal

^e Centro de Ciências e Tecnologias Nucleares, Instituto Superior Técnico, Universidade de Lisboa, E.N. 10 ao km 139, 7, 2695-066 Bobadela LRS, Portugal

^f Instituto de Plasmas e Fusão Nuclear, Instituto Superior Técnico, Universidade de Lisboa, E.N. 10 ao km 139, 7, 2695-066 Bobadela LRS, Portugal

^g National Institute of Material Physics, 405A Atomistilor Street, 077125 Bucharest-Magurele, Romania

^h Laser Department, National Institute for Laser, Plasma, and Radiation Physics, Magurele, Romania

ⁱ Institute for Nuclear Research, Pitesti, str. Campului, nr.1, Mioveni, Arges, Romania

^j Escola Básica e Secundária de Arga e Lima, 4925-404 Lanheses, Portugal

^k Transilvania University of Brasov, Centre Product Design for Sustainable Development, Eroilor 29, 500036 Brasov, Romania

ARTICLE INFO

Keywords:

Carbon coatings
Hardened steel substrate
Wear resistance

ABSTRACT

This paper presents an evaluation regarding the influence of substrate material characteristics and deposition parameters on the tribological behaviour of carbon-based coatings. Chromium nitride ceramic interlayers and carbon-based thin films were deposited by magnetron sputtering on hardened AISI 5115 (16MnCr5) case hardening steel. The physical vapour deposition (PVD) deposition was performed at three different temperatures: 180 °C, 200 °C and 250 °C. The chemical composition of the samples was assessed by Rutherford Backscattering Spectroscopy (RBS), the structure by X-ray Diffraction (XRD), and the surface morphology by Atomic Force Microscopy (AFM). The surface chemistry was analysed by X-ray Photoelectron Spectroscopy (XPS) and Raman Spectroscopy. The coatings are homogeneous, amorphous, with a smooth surface. The mechanical behaviour has been assessed on a pin-on disk rotational tribometer (wear characteristics), on a micro scratch tester (adhesion to the substrate), by ball-cratering (film thickness) and by nanoindentation (hardness and the modulus of elasticity). A strong correlation has been observed between the substrate characteristics and, more importantly, the deposition temperature, and the mechanical properties of the assembly. The fracture toughness is positively influenced by the presence of the ceramic chromium nitride interlayer. The modulus of elasticity and friction coefficient (both in dry and lubricated conditions) are decreased for higher deposition temperatures, however the higher deposition temperature negatively affects the mechanical characteristics of the steel substrate.

1. Introduction

Carbon-based thin films, either hydrogenated or doped with certain metals, can be widely used especially for tribological applications, due to their excellent mechanical and wear behaviour properties [1–3]. These types of thin films are deposited since the early seventies, using various deposition techniques [4–6]. Physical Vapor Deposition (PVD) methods are commonly used due to their relative simplicity, flexibility,

low-temperature during deposition, relatively high deposition rate, etc. [7–9]. Generally, carbon-based films exhibit low adherence to metallic substrates due to their high internal stress and low thermal stability [10,11,14–18]. Therefore, several approaches, such as the insertion of transition interlayers/multilayers between the films and the substrate, diffusion or doping processes have been tried up to date [11–14]. The influence of the doping effects of different elements (Si, W, Ti, Zr) on the micro-structural, mechanical and corrosive behaviour of carbon-

* Corresponding author.

E-mail address: camelia.gabor@unitbv.ro (C. Gabor).

<https://doi.org/10.1016/j.apsusc.2019.01.028>

Received 14 September 2018; Received in revised form 28 December 2018; Accepted 3 January 2019

Available online 04 January 2019

0169-4332/ © 2019 Published by Elsevier B.V.

based films [19,20] were reported. Guojia et al. report a positive influence of Ti and Zr dopants on the properties of carbon-based films produced by reactive magnetron sputtering with plasma ion implantation [20]. Also, the positive influence of adhesive silicon-containing interlayers deposited at different processing temperatures (100–550 °C) and deposition periods, on the tribological behaviour of carbon-based thin films deposited on steel by EC-PECVD, was presented by F. Cemin et al. [21]. Regarding the adhesion of the coatings to the substrate, an increase of the critical load necessary for film failure was reported at temperatures above 300 °C. The tribological behaviour of carbon-based thin films deposited at different temperatures (from 100 to 500 °C) was presented by Numan Salah et al. [22]. The authors report the surface roughness increase as a result of the significant morphological changes in the thin films with the deposition temperature, namely particle size increase from 10 nm to 30 nm, resulting in higher friction coefficients and wear rates [22]. The adhesion of soft and thick carbon-based films was also studied [23,24], and it was reported to be improved by a nitriding process [23,25]. Several reports regarding the effect of Cr doping on the films' adherence to the substrate can also be found in the literature [8,22,26–29]. Wang Hong-mei et al. used magnetron sputtering to obtain carbon films containing Ti, or Ti and Cr. It was shown that the Cr content improved the hardness, the modulus of elasticity and the roughness, but reduced the wear resistance of the films [8]. The influence of the Cr content (from 5 to 20 at %) on the micro-structural and tribological properties of DLC-Cr (a:C-Me) thin films was presented by S. Gayathri et al. Better friction coefficients were reported for lower Cr content while higher adhesion was obtained at higher metal concentration. The recommended optimum Cr content was at 10 ÷ 15 Cr at % [26].

This work presents the results concerning the wear behaviour improvement for a particular application in the field of textile industry, namely the bobbin case of sewing machines. The bobbin case together with the hook body, the cover ring, the needle guard and the leaf spring are the main components of the rotary hooks. The hook has an important role to stitch formation and therefore it is considered the main part of the sewing machine. The rotating hook and the bobbin case are shown in Fig. 1. The frequency of rotations of the hook during the sewing process (more than 2500 rot/min) leads to a strong wear stress between the parts being in movement and also between the thread and the hook (Fig. 2). Some special sewing machines, such as those for automotive airbags, are designed to run without lubrication, or with minimal lubrication in the rotary hook area, in order to avoid staining the thread. The bobbin case material for this case study is AISI 5115 (16MnCr5) hardened steel. Carbon-based thin films were deposited by magnetron sputtering, at three different deposition temperatures: 180, 200 and 250 °C, with or without a chromium nitride interlayer between the carburized substrate and the wear resistant coating. The main issue that needs to be addressed is the balance between the coating deposition parameters, on one hand, and the processing parameters applied on the substrate material (i.e. thermal treatment), on the other, in order

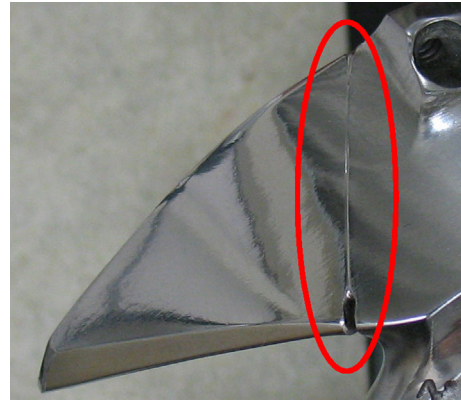


Fig. 2. Wear damage caused by the thread on a used bobbin case.

to obtain optimal performance for this particular type of application, where lubrication is highly undesirable.

2. Experimental details

2.1. Substrate preparation and characterization

The substrates were machined in cylindrical blocks, with 40 mm diameter and 15 mm height, from case hardening steel AISI 5115 (16MnCr5), the same steel which is used for the bobbin case. This steel has the Ac3 point at 835 °C, Ac1 point at 740 °C and the martensite start point (Ms) at 400 °C [30]. The substrate cylinders were case hardened to a depth of 0.5 mm, carburized, quenched and tempered to a hardness between 720 and 740 HV₅. The heat treatments (quenching/carburizing followed by tempering) were carried into a multipurpose controlled atmosphere batch furnace (CBUT 10), electrically heated and with an integrated quenching system. The atmosphere inside the furnace is composed of N₂ (1.2 m³/h) and methanol (CH₃-OH, 0.001 m³/h). For the carburizing stage, methane (CH₄) is added. The carburizing parameters were the following: carburizing temperature = 920 °C; soak time (carburizing and diffusion) = 110 min; C-potential = 0.8 ÷ 0.9%; hardening temperature = 820 °C; soak time = 10 min; quenching oil temperature = 70 °C. After quenching, the samples were cooled to room temperature, tested in terms of hardness, followed by tempering. The tempering parameters were the following: temperature = 180 °C; soak time = 60 min. The carburizing process results were assessed by testing the Vickers hardness (HV) using a CV-410 DAT hardness tester, with a 5 kgf load, in at least 4 points, separated by at least 2.5 indentation diagonals. The microstructure of the substrates after the heat treatment sequence was assessed by optical microscopy (Leitz Metallux II microscope). The substrate samples were etched using 3% Nital, for 3–5 s. The quenching depth was profiled by cross-sectional microhardness testing, with an INSTRON WOLPERT V-TESTOR 4021

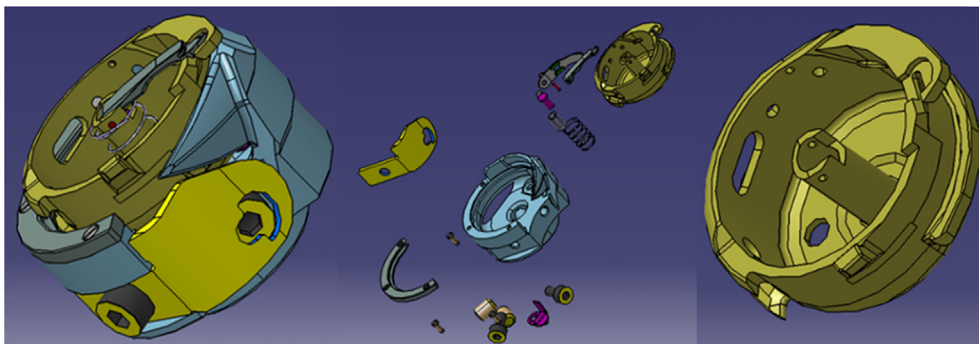


Fig. 1. Rotating hook (explosion view) bobbin case.

microhardness indenter. After the heat treatment sequence, the specimens (steel substrates) were grinded, followed by sand blasting with 40–60 μm diameter glass pearls, and afterwards polished, cleaned and ultrasonically degreased, in preparation for the coating deposition. The preparation stages of the cylindrical substrates were identical to the ones employed during production, on the bobbin cases.

2.2. Coating preparation and characterization

The films were deposited on the thermally treated AISI 5115 substrates by reactive magnetron sputtering, at different deposition temperatures: 180 °C, 200 °C, and 250 °C using high purity C targets, as well as Cr targets. The Cr target was used for the deposition of a chromium nitride interlayer in film S1, and for doping the carbon-based samples (S2 and S3). Ar was used as plasma gas (50 l/cycle). The chromium nitride interlayer of film S1 was deposited as a means to improve the adhesion to the substrate of the carbon coating [31]. Moreover, on the samples deposited at 200 °C and 250 °C, two different polarization voltages were used (–35 V and –70 V), in order to observe the influence of this parameter on the coating characteristics (adhesion to the substrate, compactness, etc). Supplementary information regarding the deposition parameters can be found in Table 1.

The atomic composition of the coatings was measured by Rutherford Backscattering Spectrometry (RBS): RBS and ERDA (Elastic Recoil Detection Analysis) measurements made at the CTN/IST Van de Graaff accelerator, with 2 MeV $^4\text{He}^+$; angle of incidence 76°; RBS detected at 160° in the Cornell geometry; ERDA spectra collected with the mobile detector located at 24° angle with the beam. RBS measurements were made in a small chamber where three detectors are installed: standard at 140°, and two pin-diode detectors located symmetrical to each other, both at 165° (detector 3 on the same side as standard detector 2). The spectra were collected for 2 MeV $^4\text{He}^+$, with a normal incidence of 25°. The RBS data were analysed with the IBA DataFurnace NDF v9.6i [32]. Double scattering was calculated with the algorithms given in [33]. Pileup was calculated with the algorithms given in [34].

Moreover, quantitative elemental analysis was performed by Energy Dispersive X-Ray Spectroscopy (EDX), with the sensitivity down to a few atomic percentages, (Thermo, Ultra Dry, Noran System 7, NSS Model, 2,000,000 counts/sec), attached to a Scanning Electron Microscope (SEM), Hitachi, S3400N, type II.

The structure of the deposited films was investigated by Grazing Incidence and symmetrical X-Ray Diffraction (GIXRD and XRD) with an instrument (Empyrean, Panalytical) working with Cu K α radiation in a parallel beam geometry, with a mirror and a 1/8° slit in the incident beam side and a 0.27° parallel beam collimator in the diffracted beam side. The step size was 0.03° and the time per step was 2 s.

The chemical composition of the deposited films was studied using X-ray Photoelectron Spectroscopy (XPS) with an ESCALAB 250Xi instrument (Thermo Fisher Scientific, Pittsburgh, PA) equipped with a monochromatic aluminium anode as the X-ray source. Wide range analyses (survey scans) were initially acquired from the surface of the deposited film with an electron pass energy of 50 eV and step size of 0.5 eV. High resolution scans for detailed peak analysis were performed at an electron pass energy of 20 eV and an energy step size of 0.1 eV. XPS spectra were acquired from as-received surface and after sputtering with Ar ions (2 keV) to reach the bulk of the deposited carbon-based thin films. To reach the interlayer from sample S1, the surface was first

mechanically polished and then sputtered with 4 keV Ar ions until the N signal from the CrN layer was detected. Afterwards, several depth sputtering cycles with lower energy Ar ion sputtering to reduce ion induced artefacts were acquired to check the homogeneity of this layer.

Raman spectra were acquired at room temperature by a triple monochromator Jobin Yvon T64000 spectrometer using the 514.5 nm line of an argon ion laser. The measurements were performed with a BHSM Olympus microscope using x100 MS Plan objective.

The atomic force microscopy (AFM) measurements were performed with a Nanonics4000 Multiview System in order to obtain the parameters as roughness average (Ra) and surface kurtosis (Rku) for the investigated samples. The AFM system works in intermittent mode and the images were collected on 20 μm \times 20 μm area, in phase feedback, using a Cr coated glass tuning fork probe (10 nm tip diameter, 38.34 kHz resonance frequency and 2000 quality factor).

The surface and cross-section morphology were analysed by SEM, using a JSM5200 electron microscope (JEOL).

The mechanical properties of the coated samples were assessed by nanoindentation, scratch resistance and wear tests. Prior to the nanoindentation tests, the coating thickness was measured by ball cratering (CSM Instruments/Anton Paar Calotest, 20 mm diameter steel erosion ball, ultrafine diamond slurry with particles smaller than 0.2 μm). The coating thickness is needed in order to minimize the substrate effect on the nanoindentation results. As specified by ISO 14577/4 (Metallic materials — Instrumented indentation test for hardness and materials parameters — Part 4: Test method for metallic and non-metallic coatings), the indentation load or displacement has to be chosen in a manner that the substrate will not have a perceivable effect on the results, the penetration depth being generally recommended to be at a maximum of 10% of the total coating thickness. Nanoindentation measurements were performed using an NHT² nanoindenter from CSM Instruments/Anton Paar, in at least 40 points for each sample, for statistical relevance. The nanoindentation parameters were the following: Berkovich diamond tip, linear loading, loading rate 5 mN/min, unloading rate 20 mN/min, no dwell time, approach speed 2000 nm/min. The parameters of interest are H_{it} (instrumented indentation hardness), and E_{it} (instrumented indentation elastic modulus). The hardness and elastic modulus were determined following the model of Oliver & Pharr [35]. The load resolution of the apparatus is 40 nN, with a usable indentation load range between 0.1 and 500 mN. The thermal drift (contractions or expansions of the sample, sample holder, indenter shaft, caused by temperature variations), which can influence the measurements with low indentation depths, is countered with the use of a zirconium reference ring, which is in contact with the sample surface. The actual indenter displacement is therefore measured between the zirconium reference ring and the indenter tip, on the shortest possible path. The reference ring also acts as a local environmental enclosure to passively protect the measurement location from air currents, sound waves and changes in humidity and temperature.

The assessment of the adhesion to the steel substrate for the coatings was performed by scratch tests, on a Micro Scratch Tester (CSM Instruments/Anton Paar) using a diamond tipped indenter with a Rockwell geometry (tip radius = 100 nm). The load was applied progressively, from 0.03 N to 30 N, with a loading rate of 10 N/min, on a length of 3 mm. Five tracks were made on each sample, and the values for the critical loads were averaged. The critical load values were obtained after optical analysis of the scratch tracks. The critical loads are

Table 1
Coating deposition parameters.

Sample	Deposition temperature	Deposition chamber	Layer	Sputtering	Working pressure
S1	180 °C	Ceme-Con C800/9XL	CrN + carbon	2Cr and 2C targets – sequential sputtering, first CrN, then carbon coating	3×10^{-3} Pa
S2	200 °C	Eifeler Vacotec Alpha 400C	carbon-based	1 Cr and 3C targets – simultaneous sputtering	
S3	250 °C	Eifeler Vacotec Alpha 400C	carbon-based	1 Cr and 3C targets – simultaneous sputtering	

defined as follows: Lc1 – the load necessary for the emergence of the first cracks in the film; Lc2 – the load corresponding to the first delamination of the film; Lc3 – the load responsible for the delamination of more than 50% of the film from the wear track. No cracks were observed on the samples, prior to partial delamination. The fracture toughness was evaluated by indentation method on a Vickers hardness tester (CV Instruments – CV700) using a load of 300 g.

Considering the requirements of the application, meaning that the coating should not be lubricated, due to the fact that the thread might be stained by the lubricant and the wear particles, the wear behaviour was performed in dry conditions. A CSM Instruments/Anton Paar rotation tribometer was used, with the following conditions: a 6 mm diameter AISI 52100 quenched steel pin, positioned at 45° relative to the sample surface, as a friction couple; 20 N applied load, stop condition 11,000 m. Three wear tracks were made on each sample. The samples and steel pins were cleaned in an ultrasonic bath, and with ethanol, directly on the tribometer, followed by compressed air blowing, in order to remove surface contaminants. The variation of the friction coefficient as function of time, distance and number of cycles, was registered by a LVDT (linear variable differential transformer) sensor, directly by the tribometer, while the wear coefficient K , calculated with Eq. (1) (where V is the volume of dislodged material in mm^3 , l is the length of the test in meters, and F is the applied load, in N), was obtained with the help of a Taylor-Hobson Surtronic 25 profilometer. The variation of temperature and humidity inside the tribometer enclosure was monitored with a Rotronic HygroFlex monitor.

$$K = \frac{V}{F \times l} \quad (1)$$

3. Results and discussions

3.1. Substrate properties: Structural evaluation and hardness

The carbon-rich layer obtained by the thermochemical treatment of AISI 5115 steel presents a martensite rich structure, with lighter-coloured carbides (chromium, manganese) at the grain boundaries (Fig. 3). The base material presents bainite sheaves with average length

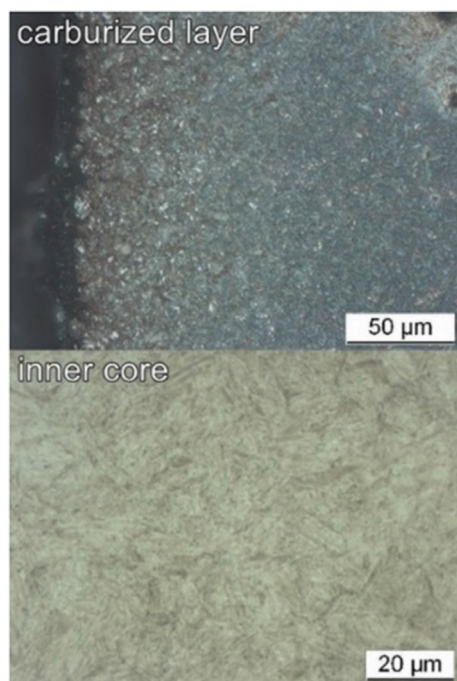


Fig. 3. Structural features of the carburized layer and of the inner core of the AISI 5115 samples, after the heat treatment sequence.

of 20 μm and thickness of 5 μm , composed of ferrite, separated by cementite and/or martensite (appearing as darker-coloured needles in Fig. 3). The residual austenite content was kept at a minimum, starting from the operational parameters of the carburizing process (i.e. the low amount of carbon (0.8% wt.) of the carburizing atmosphere, and the sufficient amount of time allowed for carbon diffusion). The microhardness profile HV_1 (according to DIN EN ISO 6507-1) of the carburized samples has indicated an average layer thickness of $520 \pm 10 \mu\text{m}$. After quenching, the average microhardness value of the carburized layer was $805 \pm 4.3 \text{ HV}_5$. After the tempering stage, the hardness of the substrate dropped to $732 \pm 3.39 \text{ HV}_5$.

3.2. Coating chemical composition, morphology and structure

The chemical composition of the samples, in cross section, is presented in Fig. 4. The in-depth chemical composition of Sample S1 is homogeneous, the C and H content are relatively stable until the substrate is reached. Argon entrapment is noticeable. Considering the carbon/hydrogen ratio, the coating on sample S1 can be considered as hydrogenated carbon. For samples S2 and S3, one can notice slight elemental composition deviations, especially at the surface of the coatings, mostly due to the entrapment of hydrogen and argon, as a result of the deposition process, as well as significant traces of oxidation. Towards the substrate, the chromium and hydrogen content decreases, while the carbon content increases. Moreover, one can notice slight traces of copper. The presence of copper and higher oxygen content can be explained by the fact that the samples were cross-sectionally cut by electro-erosion, in order to preserve the integrity of the coating/substrate interface. Gaseous contamination appears due to the oxidation and reduction processes during electro-erosion primarily located in the vicinity of the electrodes (the sample and the copper wire) [36]. Considering the chemical composition of samples S2 and S3, the coatings can be considered a:Cr-Me films, where Me = Cr. Considering the relatively low difference in mass for C and N, and between Fe and Cr, the chromium nitride interlayer is not clearly visible on the RBS spectra. However, supplementary analyses by EDX were made on the substrate, interlayer and film on the top, for sample S1, confirming the proportions obtained from RBS. In case of the chromium nitride interlayer, the composition is: 23.75 N at %, 60.28 Cr at %, with traces of carbon due to the erosion process during ball cratering.

The XRD patterns of the samples, shown in Fig. 5, indicate the presence of a diffraction peak at $\sim 45^\circ$ which could be ascribed to the ferrite solid solution from the AISI 5115 steel substrate. Compared to the symmetrical configuration, once the omega angle is decreased in the GIXRD configuration, the intensity of the diffraction peak situated at $\sim 45^\circ$ is significantly reduced, an observation which confirms the previous statement. Consequently, the amorphous nature of the films is confirmed. There are no obvious diffraction peaks which could be ascribed to carbon in the carbon coatings, so it could be concluded that carbon is present in a dominantly amorphous form in the coatings. The diffraction peak located at $2\theta = 38.79^\circ$, noticed on the patterns of sample S1, could be attributed to the chromium nitride interlayer, due to diffraction on the (1 1 1) planes of the fcc CrN phase (04-015-3258) or the (0 0 2) planes of the hex - $\text{Cr}_2\text{N}_{0.95}$ phase (01-083-5615). The chemistry of the coatings and interlayer, obtained by XPS and Raman spectroscopy, will be presented in the following sections.

Fig. 6 presents the in-detail C1s XPS spectra of the films surface, after they were subjected to the Ar-sputtering contaminants removal procedure. The deconvolution of the C1s spectra was performed with Gaussian-Lorentzian shapes, and the relative percentage has been indicated for each carbon hybridization state. The band corresponding to C (sp^2) is located at $\sim 284.8 \text{ eV}$, while the band ascribed to C (sp^3) could be found at 285.8 eV in all the analyzed samples. Also, the bands at 288.1 eV and 289.1 eV could be ascribed to the presence of C=O and O=C–O bonds, indicating a low oxidation degree of carbon, possibly due to the chemisorbed oxygen.

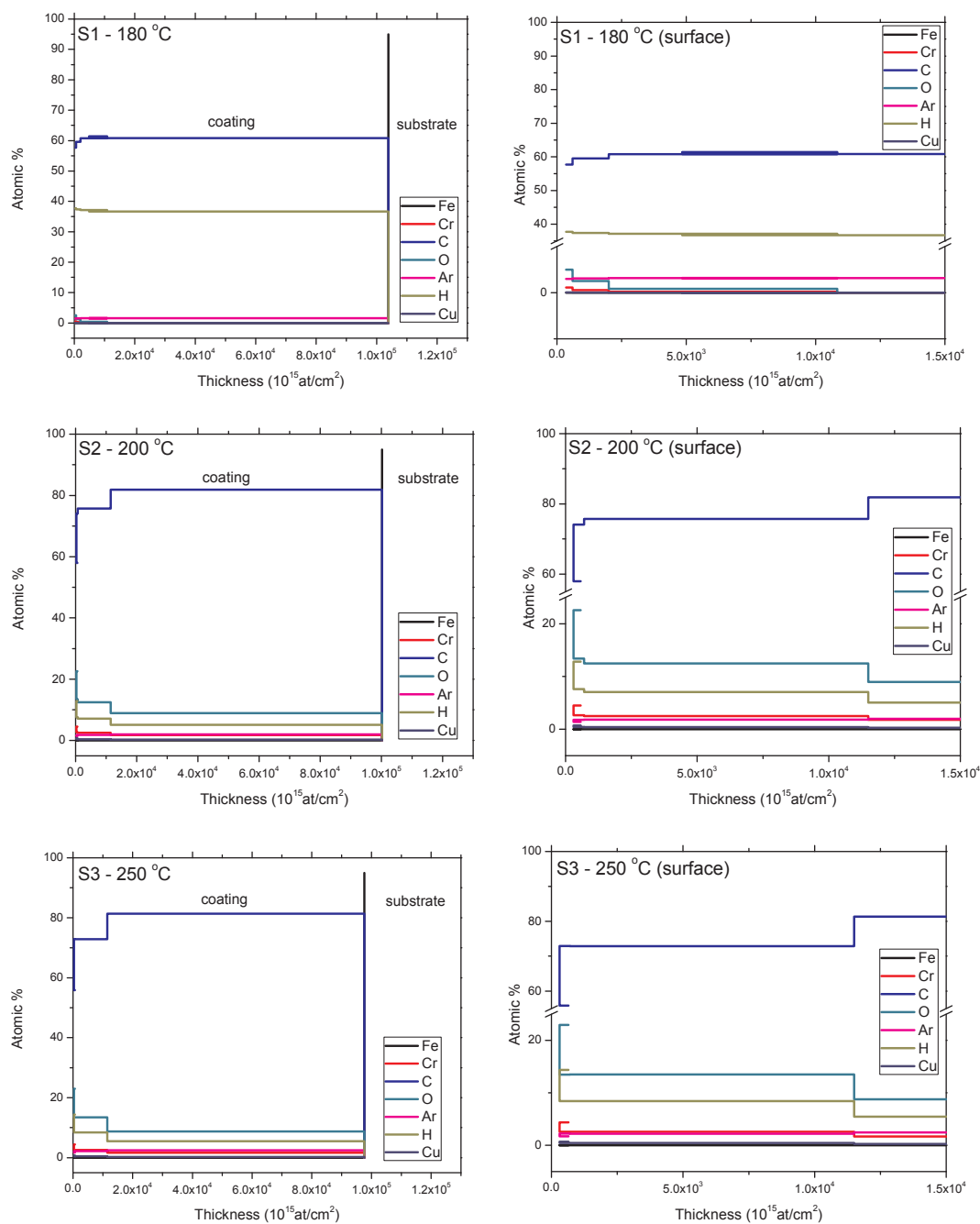


Fig. 4. The variation of atomic percentages as function of depth, for the surface region and the coating/substrate system. The transition between the coating and the substrate is clearly visible.

The relative amount of the hybridization states of carbon are important to describe the behavior of the sputtered films. A higher sp^3/sp^2 ratio signifies a more diamond-like chemistry of the coating, while low sp^3/sp^2 ratios are responsible for a graphite-like chemistry. The dominating contribution in all films is attributed to the sp^2 hybridization state, however, the relative sp^3/sp^2 ratio increases from 0.16 in the case of S1 to 0.28 and 0.30 for S2 and S3, respectively.

In the case of samples S2 and S3, a supplementary peak is located at 283.8 eV, which corresponds to chromium carbide, thus a part of the carbon atoms is bonded to the chromium atoms [44].

Considering that from the XRD analysis regarding sample S1, one supplementary diffraction peak was observed at $2\theta = 38.79^\circ$, which was proposed to be attributed to the chromium nitride interlayer, further XPS investigations were performed, in order to confirm or deny

this supposition. Firstly, the sample was mechanically polished gradually, in order to remove the carbon-based top layer and to reveal the interlayer. As it can be observed in Fig. 7, the Cr2p and N1s XPS spectra (Fig. 7a, b) confirm the presence of chromium and nitrogen inside the interlayer coating for sample S1. The sputter-depth profile through the intermediate layer shown in Fig. 7a, b was performed for a total time of 10 min, with acquisition of the spectra at 1 min intervals, suggesting a constant chromium and nitrogen content over the entire sputter time. Moreover, by accessing the subsurface region, a N1s core-level shift to higher binding energy is observed (Fig. 7b), most noticeable between the “as-received” spectra and the “1 min-sputtered” spectra. This chemical effect occurs between the surface and near-surface atomic layers indicating a modification of the chemical environment.

In order to further explore the chemical composition of the

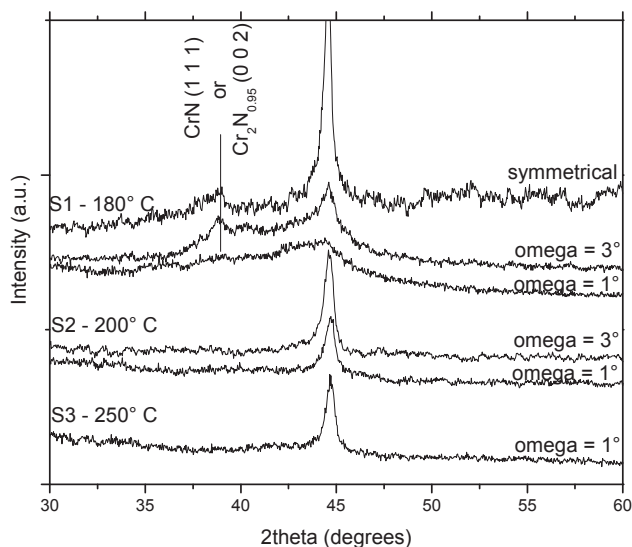


Fig. 5. XRD patterns (symmetrical and glancing angle).

intermediary layer of sample S1, the deconvolution of $\text{Cr}2p_{3/2}$ and $\text{N}1s$ photoelectron lines was done following the recommendations found in [38]. Fig. 7c–h, Tables 2 and 3 display chromium and nitrogen chemical species together with their concentrations, in very good agreement with the chemical assignments given in the literature [38–40], thus confirming the observation from the XRD analysis. The metallic feature increases with depth accompanied by the decrease of chromium nitrides and oxides (Table 3). The nitrogen chemistry (Table 4) illustrates a dominant contribution of CrN (~80%) on top of the surface before the ion sputtering. By increasing the sputtering time, Cr_2N chemical feature increases with the decrease of chromium oxynitride contribution (Table 4). It is worth stressing that element relative concentrations (Table 2) are consistent with these findings. Thereby, quantitative analysis strengthens the above observations regarding the chemical behavior across the surface and subsurface region, highlighting the tendency of Cr_2N formation with depth.

Fig. 8 shows the Raman spectra of the samples in the region between 900 cm^{-1} and 1800 cm^{-1} , where two-bands features are clearly seen. The higher frequency band ($\sim 1580\text{ cm}^{-1}$) and the lower frequency band ($\sim 1360\text{ cm}^{-1}$) are generally recognized as the G and D band, respectively, for carbon materials. The G band is associated with the overrending vibration of the longitudinal optical branches of hexagonal graphite (Csp^2) while the D Raman phonon band could be ascribed to a disordered structure (Csp^2). Qualitative information has been extracted from the Raman spectra by fitting the D band with a Lorentzian curve profile and the G band with an asymmetric Breit–Wigner–Fano (BWF) [41] curve profile, which is described by Eq. (2). The results for the fitting parameters are summarized in Table 5.

$$I(\omega) = \frac{I_0 \left[1 + \frac{2(\omega - \omega_0)}{Q\Gamma} \right]^2}{1 + \left[\frac{2(\omega - \omega_0)}{\Gamma} \right]^2} \quad (2)$$

where $I(\omega)$ is the calculated Raman intensity, $1/Q$ is an asymmetric parameter which is a measure of the interaction of the phonons with a continuum of states, ω_0 , I_0 and Γ are the BWF peak position, intensity and the full width at half maximum (FWHM), respectively. The G band position is located at ω_{max} :

$$\omega_{\text{max}} = \omega_0 + \frac{\Gamma}{2Q} \quad (3)$$

From Fig. 8 it is seen that the overall Raman intensity decreases for the samples S2 and S3, in comparison with S1. This behavior could be attributed to an increase of the surface reflectivity due to the

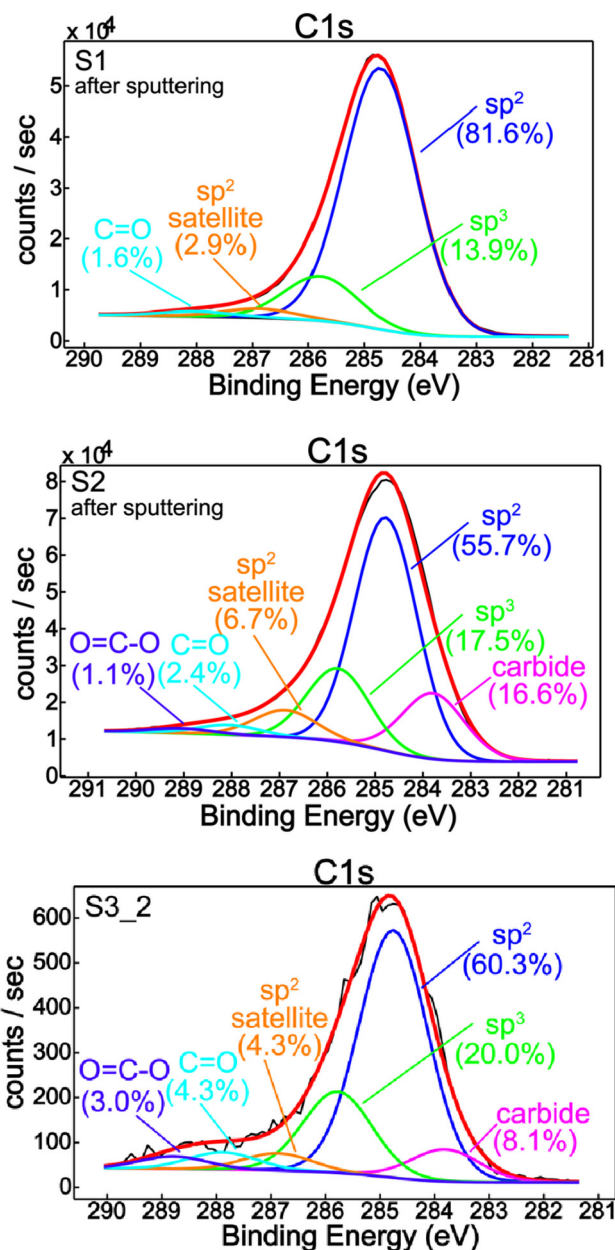


Fig. 6. XPS $\text{C}1s$ deconvoluted spectra.

incorporation of the chromium atoms in the a: C-H matrix [42,43]. The decreasing of the ω_{max} , the broadening of the G band, that is due to the clusters size, cluster distributions and lattice distortions as well as the increase of the $I(D)/I(G)$ are the other observations that are related with the incorporation of metal atoms in the a: C-H matrix [2].

AFM topography images indicate the presence of a low roughness smooth surface for the coatings, with maximum grain sizes of $1\ \mu\text{m}$. No obvious modifications in morphology were observed among the three carbon-based layers. Moreover, from the AFM images (Fig. 9), recorded on $20\ \mu\text{m} \times 20\ \mu\text{m}$ area, it can be observed that at this scale the samples are characterized by a grainy morphology. The R_a parameter interpolated from AFM shows that the differences between the coatings is not significant, mainly between S2 ($R_a = 18.5\ \text{nm}$) and S3 ($R_a = 17.9\ \text{nm}$), which means that the roughness is not affected by the increase of the temperature in the range $180\text{--}250\text{ }^\circ\text{C}$. Regarding the surface kurtosis parameter (R_{ku}) which indicates if we have samples characterized by sharp peaks, the obtained value ($R_{ku} = 6.1$) shows that in the case of S1 at the surface some large peaks (grains) are

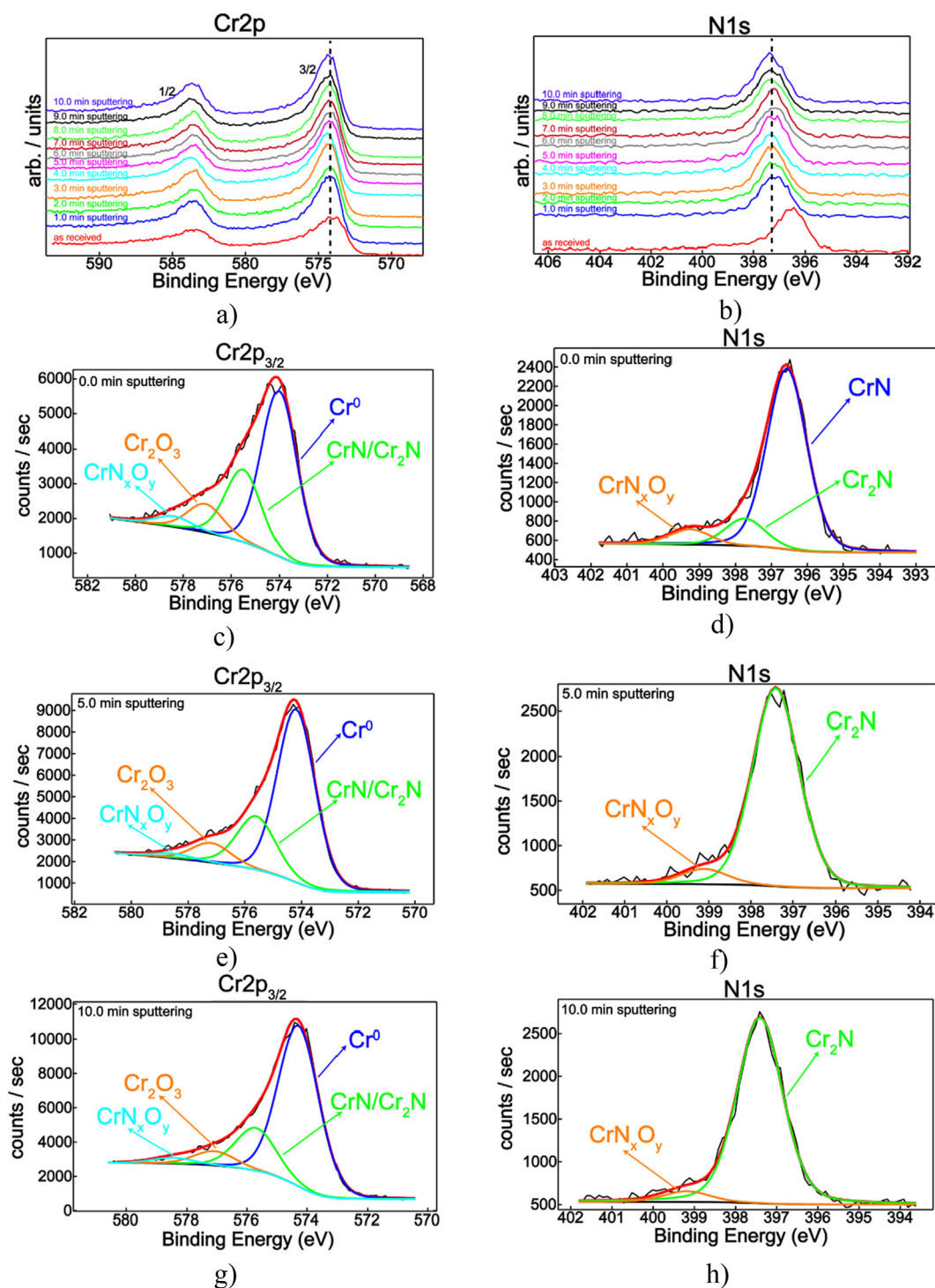


Fig. 7. XPS in-depth spectra: (a) Cr2p; (b) N1s. Cr2p_{3/2} and N1s XPS deconvoluted spectra: (c), (d) 0.0 min sputtering; (e), (f) 5.0 min sputtering; (g), (h) 10.0 min sputtering.

Table 2
Relative elemental concentrations (at. %).

Sputter time (min)	O1s	C1s	Cr2p	N1s
0.0	12.6	41.2	22.0	24.2
5.0	4.3	32.1	35.3	28.3
10.0	4.8	30.5	39.6	25.1

formed. This remark is sustained by the S1 AFM image. It can be also observed that sample S2 is characterized by a greater number of peaks in comparison with S3 which is reflected in the Rku values determined for these samples (5.7 for sample S2 and 5.1 for sample S3).

The SEM images in Fig. 10 reveal the formation of very smooth, continuous and homogenous coatings with no apparent porosity on the substrate steel surface. Moreover, Fig. 7 depicts an apparent adequate adhesion between the wear resistant coatings and the steel substrate. This behaviour can be due to the low amount of oxygen content at the interfacial layer and rich carbon content at the top of the coating. One

Table 3
Chromium chemistry: Binding energies, surface chemical species, chemical states relative concentrations.

Sputter Time (min)	Chromium chemical species	Binding energy (eV)	Chromium chemical states relative concentrations (%)
0.0	Cr ^{metallic}	574.0	58.9
	CrN/Cr ₂ N	575.5	26.6
	Cr ₂ O ₃	577.1	10.6
	CrO ₃	578.4	3.9
5.0	Cr ^{metallic}	574.2	67.0
	CrN/Cr ₂ N	575.6	23.0
	Cr ₂ O ₃	577.2	8.0
	CrO ₃	578.5	2.0
10.0	Cr ^{metallic}	574.3	71.4
	CrN/Cr ₂ N	575.7	19.6
	Cr ₂ O ₃	577.1	6.4
	CrO ₃	578.5	2.6

Table 4
Nitrogen chemistry: binding energies, surface chemical species, chemical states relative concentrations.

Sputter time (min)	Nitrogen chemical species	Binding energy (eV)	Nitrogen chemical states relative concentrations (%)
0.0	CrN	396.6	80.8
	Cr ₂ N	397.7	12.4
	CrN _x O _y	399.3	6.8
5.0	Cr ₂ N	397.4	92.5
	CrN _x O _y	399.1	7.5
10.0	Cr ₂ N	397.4	94.5
	CrN _x O _y	399.2	5.5

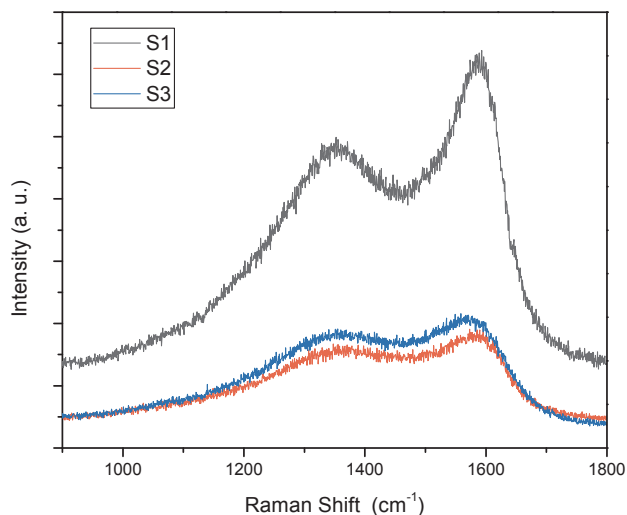


Fig. 8. The Raman spectra of the carbon-based coatings.

Table 5
Fit results from the deconvolution of the broad bands obtained from Raman analysis.

Sample	ω_{max} (cm ⁻¹)	ω_D (cm ⁻¹)	$I(D)/I(G)$	FWHM (G) (cm ⁻¹)	FWHM (D) (cm ⁻¹)	Q^{-1}
S1	1588	1341	0.68	112	253	-3.63
S2	1585	1348	0.83	133	300	-2.85
S3	1576	1339	0.78	157	283	-2.77

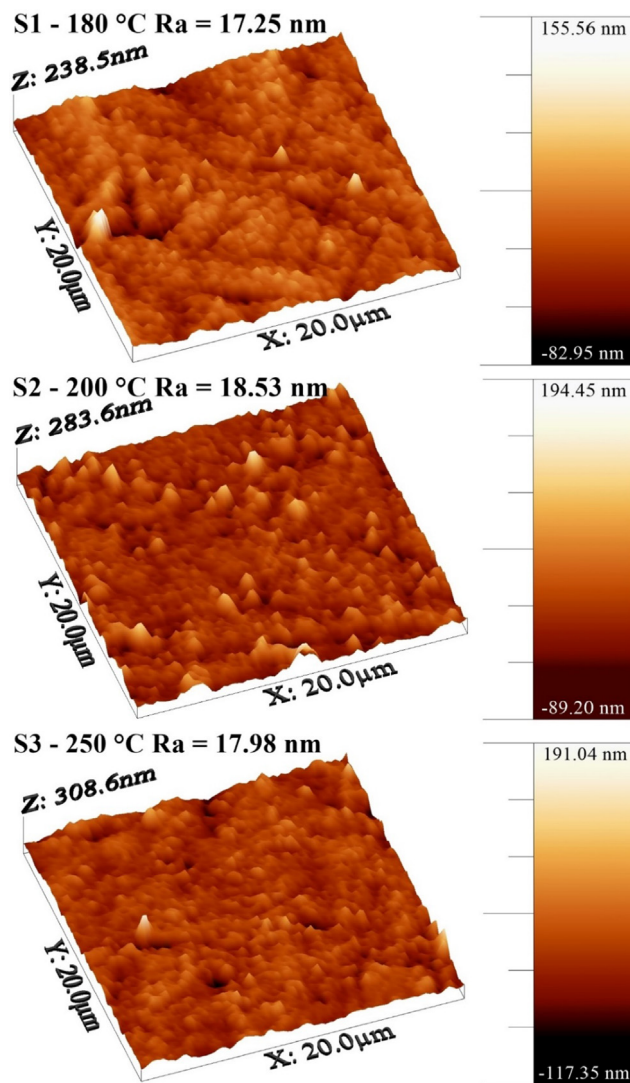


Fig. 9. AFM micrographs of the deposited coatings.

can notice that for higher deposition temperatures, for samples S2 and S3, slightly larger clusters can be observed on the surface of the coatings. This phenomenon might be explained by the fact that at elevated temperatures the germination/nucleation and growth of the particles can occur more easily. Other reports mention this phenomenon, as well [22]. The combination of the deposition parameters can lead to roughly the same coating thickness, as can be observed for samples S2 and S3. Even if the substrate bias voltage is significantly higher for S3, which would lead to a more compact and slightly thinner coating, compared to S2, a 25% increase in deposition temperature is sufficient to overcome the effect of the substrate bias voltage.

3.3. Coating/substrate system mechanical characteristics

The results from the mechanical characterization (nanoindentation, scratch resistance, and wear tests) are presented in Table 6. The first observation that can be made is that the substrate hardness is significantly affected by the deposition temperature, especially for the deposition carried out at 250 °C. For this particular deposition temperature, the hardness is decreased by 6%, compared to the hardness of the substrate after tempering. For the samples deposited at 180 °C and 200 °C, a smaller decrease in hardness is noticed. It seems that the cut-off temperature value is somewhere between 200 °C and 250 °C. The H/E ratio, called the elastic strain to failure, gives information on the wear

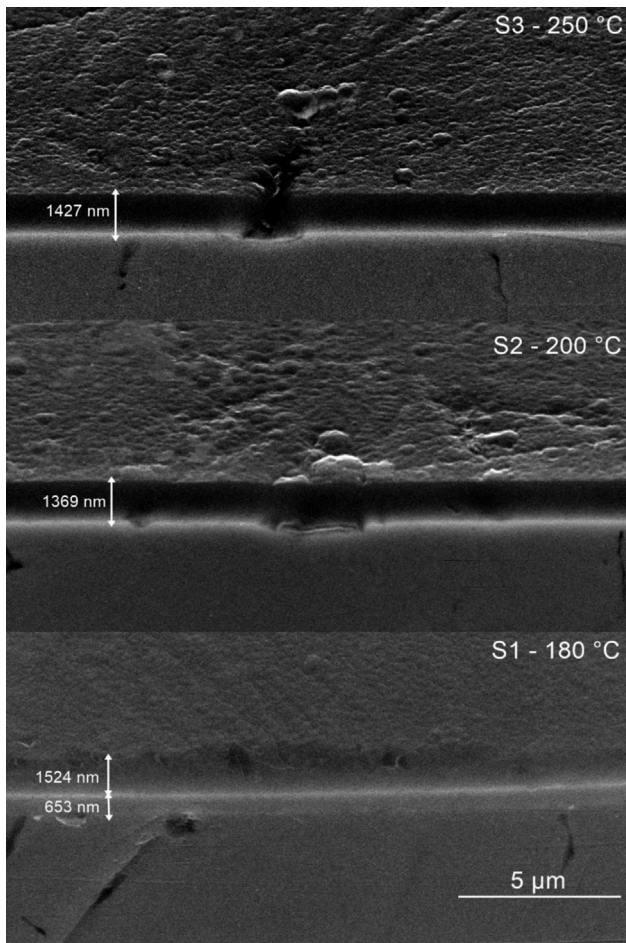


Fig. 10. Scanning electron micrographs, in cross-section.

resistance of the material in question. Higher values for this ratio, meaning a combination of high hardness and low elastic modulus, would confer the coating increased fracture toughness. Furthermore, the H^2/E^2 ratio gives information about the elastic resilience of materials (i.e. their ability to elastically absorb energy without yielding). Moreover, the H^3/E^2 ratio is an indicator regarding the material's resistance against plastic deformation. Lower values of this ratio signify a poor resistance to plastic deformation. Observing the results from Table 6, one can extract certain correlations which generally support the previously mentioned predictions. Sample S1 exhibits the highest value for the H/E ratio, which would infer better wear characteristics, compared to the remaining samples. This observation is supported by the values for the friction coefficient and especially for the wear rate, which is significantly lower than that of sample S2 and S3, $2.42 \times 10^{-8} \text{ mm}^3/\text{N/m}$, compared to $4.73 \times 10^{-8} \text{ mm}^3/\text{N/m}$ and $5.01 \times 10^{-8} \text{ mm}^3/\text{N/m}$, respectively. Moreover, an increased fracture toughness is extrapolated from the Lc2 and Lc3 critical loads, sample S1 exhibiting a higher resistance to crack formation and propagation.

Fig. 11 contains the variation of the applied force during indentation, as function of the penetration depth. From small changes in slope for the loading and unloading curves, some phenomena can be anticipated. Samples S1 and S2 exhibit on the loading curves, for loads higher than 2 mN, variations in slope (“pop-ins”) that signify that one of several phenomena can occur: micro-cracks, phase transformations, dislocations nucleation, strain transfer across grain boundaries, if the material is crystalline, all due to the applied load. Furthermore, sample S2 exhibits the same change in slope on the unloading curve, as well, which signify the occurrence of the “pop-out” effect. These occurrences are not observed on the curves obtained for sample S3. This

Table 6
Coating mechanical characteristics: HVIT – conversion to Vickers units from GPa; Hit – indentation hardness; Eit – indentation elastic modulus; COF – friction coefficient; K – wear coefficient; Lc2 – second critical load; Lc3 – third critical load.

Sample	Substrate hardness (HV _{0.05})	HVIT	Hit (GPa)	Eit (GPa)	H/E	H ² /E ²	H ³ /E ²	COF (dry)	COF (lubricated)	K (in dry conditions) mm ³ /N/m	Lc2	Lc3
S1	704.22 ± 3.85	1248.59 ± 268.35	13.48 ± 2.89	113.35 ± 16.76	0.119	0.0141	0.1906	0.12	0.08	2.42 × 10 ⁻⁸	7.93 ± 0.14	16.05 ± 1.18
CrN interlayer												
S2	703.11 ± 4.42	1490.09 ± 51.54	16.58 ± 0.55	185.57 ± 4.92	0.089	0.0079	0.1323	-	-	4.73 × 10 ⁻⁸	6.37 ± 1.23	13.21 ± 1.14
S3	688.78 ± 5.03	793.29 ± 120.34	8.56 ± 1.29	116.39 ± 29.68	0.073	0.0054	0.0463	0.15	0.10	5.01 × 10 ⁻⁸	5.77 ± 0.91	15.59 ± 0.35
* - before deposition	732 ± 3.39											

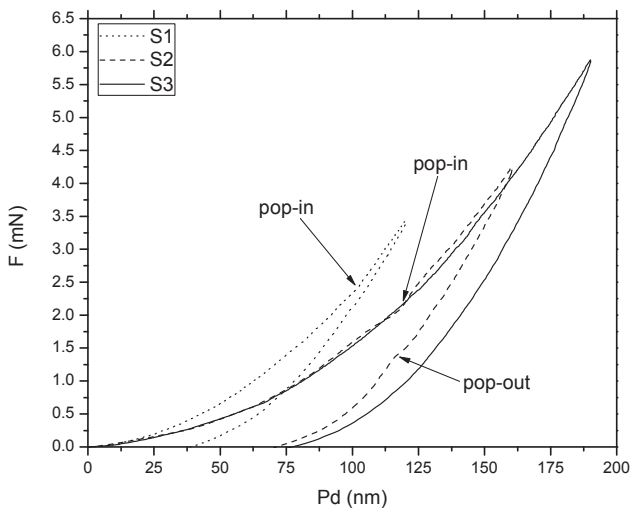


Fig. 11. Typical loading/unloading nanoindentation curves.

phenomenon might be due to the discrepancy between the values for the elastic modulus. Stiffer materials, as is the case for samples S1 and S2 ($S1 = 113.35 \text{ GPa}$, $S2 = 116.39 \text{ GPa}$), cannot accommodate the deformation without the appearance of cracks, while this accommodation may happen in less stiff materials (with lower elastic modulus values, $S3 = 97.93 \text{ GPa}$). The small area of the hysteresis between pop-in and pop-out curves reveals also the decreased capacity of plastic deformation for S1, consistent with the high values for the H/E ratio.

To further assess the fracture toughness of the coatings, a Vickers hardness tester has been used to perform indentation experiments with a load of 300 gf. The results of interest were: the shape and direction of the cracks occurring in the coating, the width of the delaminated portion at the edge of the indent, and the shape of the delaminated fragments. The indentation morphologies at the edge of the imprints are presented in Fig. 12. It can be observed that the indentation morphology of sample S1 shows large radial cracks and delaminated regions, revealing a relatively poor adhesion. However, the width of the delaminated portion is significantly reduced, compared to samples S2 and S3 ($28.43 \pm 3.23 \mu\text{m}$, versus $64.96 \pm 5.33 \mu\text{m}$, and $69.65 \pm 4.58 \mu\text{m}$). This observation implies that the chromium nitride

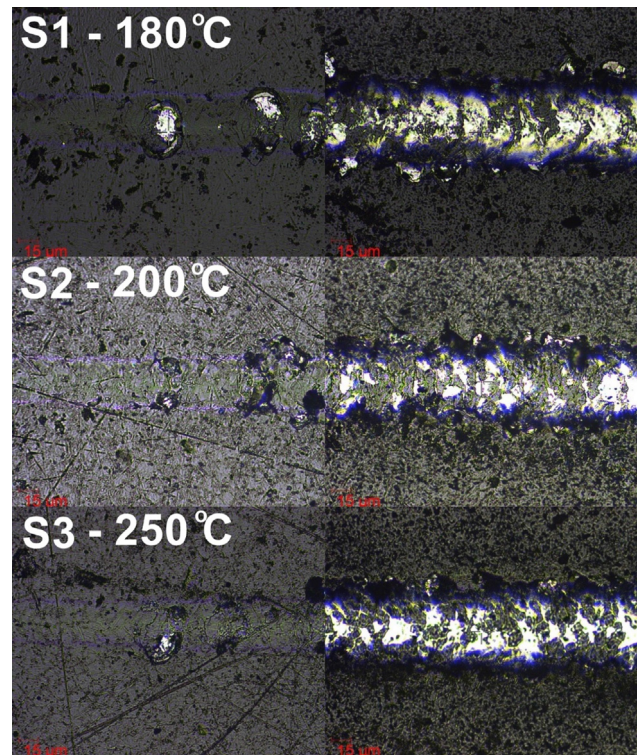


Fig. 13. Optical micrographs of scratch tracks performed on the wear resistant thin films (left side – second critical load, the first delamination; right side – third critical load, film removal).

interlayer has an important role related to the reduction of crack propagation. The relatively severe delamination exhibited by sample S1 is mainly due to the high hardness and brittle nature of the chromium nitride coating. The degree of delamination is reduced on sample S2 and especially on sample S3. The lower hardness of the substrate and coating seems to better accommodate the plastic deformation caused by the indenter. Moreover, no cracks were observed at the corners of the Vickers imprints, on all samples, signifying adequate fracture toughness of the coating/substrate system.

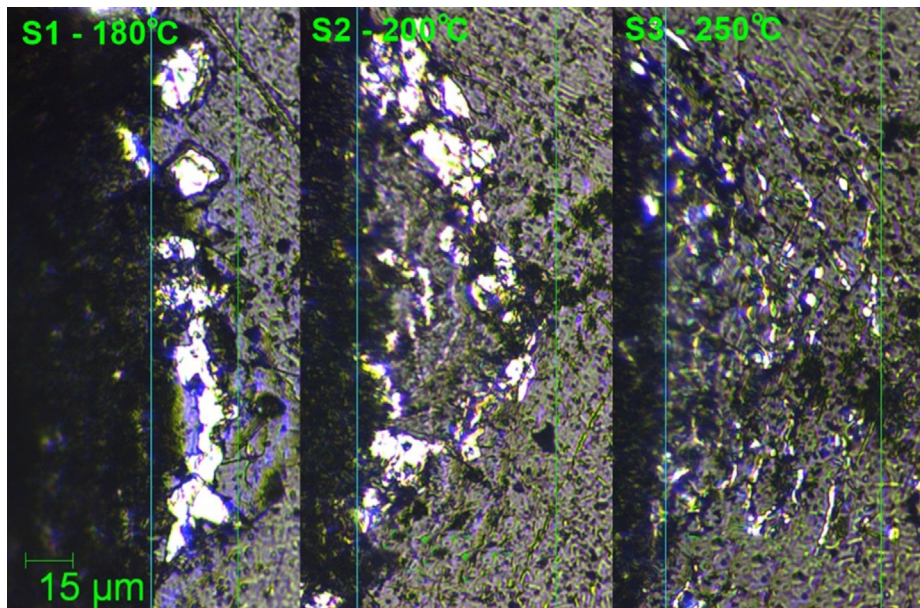


Fig. 12. Coating morphology at the edge of Vickers imprints.

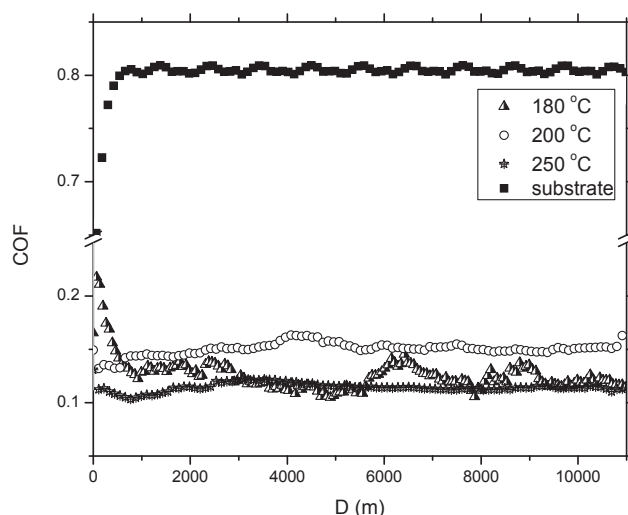


Fig. 14. The variation of the friction coefficient as function of the sliding distance.

The behaviour during scratch testing can be divided in two, for the sample deposited at 180 °C, on one hand, and the samples deposited at 200 °C and 250 °C, on the other. Thus, it would seem that the chromium nitride interlayer plays an important role in the phenomena occurring during scratch testing. It is important to mention that before the first film delamination (Lc2), on all tested samples, there were no signs of cracks (Lc1). The delaminated sections presented in Fig. 13 for S1 are indicative of wedging/spallation. This phenomenon is caused by increased stiffness of the coating, probably related to the significantly higher elastic modulus value of the chromium nitride interlayer. In this case, the coating is not capable of buckling, followed by compressive shear crack formation through the thickness of the coating. Displacements of coating sections will cause ripples in front of the indenter to spall. The delaminated regions observed for the remaining samples are indicative of recovery spallation, which is caused by the elastic recovery of the coating, occurring behind the stylus. This phenomenon is related to the degree of plastic deformation occurring in the substrate, after the stylus is passed on the surface, and also to the elastic recovery of the coating.

The variation of the friction coefficient is relatively stable for samples S2 and S3, regardless of distance, as can be observed in Fig. 14, while sample S1 exhibits a significantly larger static friction coefficient (starting point). Nevertheless, all samples have an adequate wear behaviour, characterized by low friction coefficients (S1 COF = 0.12, S2 COF = 0.15, S3 COF = 0.11) and very low wear rates (S1 $K = 2.42 \times 10^{-8} \text{ mm}^3/\text{N/m}$, S2 $K = 4.73 \times 10^{-8} \text{ mm}^3/\text{N/m}$, S3 $K = 5.01 \times 10^{-8} \text{ mm}^3/\text{N/m}$), especially compared to the bare substrate, tested in identical conditions (COF = ~0.8). The tests were repeated and results were found to be reproducible. The trend of friction value with sliding distance is different between samples. For sample S1, the friction coefficient is large at the beginning of the tests, ~0.20, and decreases gradually to a low average value of 0.12, after run-in. In contrast, samples S2 and S3 essentially do not exhibit a run-in period. The friction coefficients were small, ~0.15 and ~0.10, at the initial stage of sliding and remained at such small values for the whole sliding distance. The surface roughness values of the coatings are: S1 Ra = 17.25 nm, S2 Ra = 18.53 nm, and S3 Ra = 17.98 nm, respectively. This shows marginal differences in the roughness value. Therefore, the effect of surface roughness cannot be a deterministic factor for the comparative analysis of friction and wear in these coatings. As mentioned elsewhere [37], a regime of ultra-low friction coefficients combined with very low wear rates is generally encountered in humid atmospheres, in the case of carbonaceous coatings, due to the fact that the active dangling carbon bonds on the contact sliding surface become

passivated by hydrogen, OH groups and water molecules. Thus, a possible cause for the run-in period for sample S1 could be related to the low humidity value inside the tribometer enclosure, at 27.65%, compared to the values of Rh% for samples S2 (Rh = 41.29%) and S3 (Rh = 30.60%), respectively. Nevertheless, all coatings exhibit adequate mechanical characteristics, considering the previously mentioned application.

4. Conclusions

Wear resistant films were deposited on the thermally treated AISI 5115 substrates by reactive magnetron sputtering, at different deposition temperatures: 180 °C, 200 °C, and 250 °C using high purity C targets, as well as Cr targets, for the intermediary chromium nitride layer and the a:C-Me type films. Ar was used as plasma gas. The coatings are homogeneous, amorphous, with a smooth surface. The roughness is not affected by the increase of the deposition temperature in the range 180–250 °C. For higher deposition temperatures, slightly larger clusters can be observed on the surface of the coatings. The wear rate is low between $2.42 \times 10^{-8} \text{ mm}^3/\text{N/m}$, and $5.01 \times 10^{-8} \text{ mm}^3/\text{N/m}$. The adhesion behaviour to the substrate is closely related to the hardness and elastic modulus of the substrate, and of the interlayer and carbon coating. The higher deposition temperature negatively affects the hardness of the steel substrate, with significant effects on the performance of the entire coating/substrate system.

Acknowledgement

We hereby acknowledge the structural funds project PRO-DD (POSCCE, O.2.2.1., ID 123, SMIS 2637, ctr. no 11/2009) for providing some of the infrastructure used in this work.

References

- [1] Ana Gasco Owens, Sonia Brühl, Silvia Simison, Christian Forsich, Daniel Heim, Comparison of tribological properties of stainless steel with hard and soft DLC coatings, *Proc. Mater. Sci.* 9 (2015) 246–253.
- [2] J. Robertson, Diamond-like amorphous carbon, *Mater. Sci. Eng. R* 37 (2002) 129–281.
- [3] Dorota Bociaga, Anna Sobczyk-Guzenda, Witold Szymanski, Anna Jedrzejczak, Aleksandra Jastrzebska, Anna Olejnik, Krzysztof Jastrzebski, Mechanical properties, chemical analysis and evaluation of antimicrobial response of Si-DLC coatings fabricated on AISI 316 LVM substrate by a multi-target DC-RF magnetron sputtering method for potential biomedical applications, *Appl. Surf. Sci.* 417 (2017) 23–33.
- [4] W. Zhang, A. Tanaka, K. Wazumi, et al., Tribological properties of the diamond-like carbon films in dry and high moist air, *Tribol. Lett.* 14 (2003) 123–130.
- [5] N. Akita, Y. Konishi, S. Ogura, M. Imamura, Y.H. Hu, X. Shi, Comparison of deposition methods for ultra-thin DLC overcoat film for MR head, *Diamond Relat. Mater.* 10 (2001) 1017–1023.
- [6] W.S. Choi, K. Kim, J. Yi, B. Hong, Diamond-like carbon protective anti-reflection coating for Si solar cell, *Mater. Lett.* 62 (2008) 577–580.
- [7] Stephen Abela, *Physical Vapour Deposition on Mg Alloys for Biomedical Applications, Surface Modification of Magnesium and its Alloys for Biomedical Applications*, Woodhead Publishing Series in Biomaterials, 2015, pp. 81–100.
- [8] Wang Hong-Mei, Zhang Wei, Yu He-long, Liu Qing-liang, Tribological properties of DLC films prepared by magnetron sputtering, *Phys. Proc.* 18 (2011) 274–278.
- [9] G. Bräuer, B. Szyszka, M. Vergöhl, R. Bandorf, Magnetron sputtering - milestones of 30 years, *Vacuum* 84 (2010) 1354–1359.
- [10] C. Forsich, D. Heim, T. Mueller, Influence of the deposition temperature on mechanical and tribological properties of a-C:H:Si coatings on nitride and postoxidized steel deposited by DC-PACVD, *Surf. Coat. Technol.* 203 (2008) 521–525.
- [11] A.F.M. Borges, E. Pfender, J. Heberlein, Influence of nitrided and carbonitrided interlayers on enhanced nucleation of diamond on stainless steel 304, *Diamond Relat. Mater.* 10 (2001) 1983–1990.
- [12] V.F. Neto, R. Vaz, M.S.A. Oliveira, J. Grácio, CVD diamond-coated steel inserts for thermoplastic mould tools—characterization and preliminary performance evaluation, *J. Mater. Process. Technol.* 209 (2009) 1085–1091.
- [13] M. Jellesen, T. Christiansen, L. Hilbert, P. Møller, Erosion-corrosion and corrosion properties of DLC coated low temperature gas nitrided austenitic stainless steel, *Wear* 267 (2009) 1709–1714.
- [14] N. Ueda, N. Yamauchi, T. Sone, A. Okamoto, M. Tsujikawa, DLC film coating on plasma-carburized austenitic stainless steel, *Surf. Coat. Technol.* 201 (2007) 5487–5492.
- [15] M.M. Morshed, B.P. McNamara, D.C. Cameron, M.S.J. Hashmi, Stress and adhesion in DLC coatings on 316L stainless steel deposited by a neutral beam source, *J.*

- Mater. Proc. Technol. 141 (1) (2003) 127–131.
- [16] P. Mosaner, M. Bonelli, A. Miotello, Pulsed laser deposition of diamond-like carbon films: reducing internal stress by thermal annealing, *Appl. Surf. Sci.* 208–209 (2003) 561–565.
- [17] S. Takeuchi, A. Tanji, H. Miyazawa, M. Murakawa, Synthesis of thick DLC film for micromachine components, *Thin Solid Films* 447–448 (2004) 208–211.
- [18] A. Grill, B. Meyerson, V. Patel, Interface modifications for improving the adhesion of a-C: H films to metals, *J. Mater. Res.* 3 (2) (1988) 214–217.
- [19] M. Ikeyama, S. Nakao, Y. Miyagawa, S. Miyagawa, Effects of Si content in DLC films on their friction and wear properties, *Surf. Coat. Technol.* 191 (2005) 38–42.
- [20] Guojia Ma, Guoqiang Lin, Gang Sun, Huaifang Zhang, Wu. Hongchen, Characteristics of DLC containing Ti and Zr films deposited by reactive magnetron sputtering, *Phys. Proc.* 18 (2011) 9–15.
- [21] F. Cemin, L.T. Bim, C.M. Menezes, M.E.H. Maia da Costa, I.J.R. Baumvol, F. Alvarez, C.A. Figueroa, The influence of different silicon adhesion interlayers on the tribological behavior of DLC thin films deposited on steel by EC-PECVD, *Surf. Coat. Technol.* 283 (2015) 115–121.
- [22] Numan Salah, Ahmed Alshahrie, Javed Iqbal, P.M.Z. Hasan, M.Sh. Abdel-Wahab, Tribological behavior of diamond-like carbon thin films deposited by the pulse laser technique at different substrate temperatures, *Tribol. Int.* 103 (2016) 274–280.
- [23] E.L. Dalibon, D. Heim, Ch. Forsich, S.P. Brühl, Mechanical behavior of nitrated 316L austenitic stainless steel coated with a: C-H-Si, *Proc. Mater. Sci.* 9 (2015) 163–170.
- [24] Bernd Rübzig, Daniel Heim, Christian Forsich, Christian Dipolt, Thomas Mueller, Andreas Gebeshuber, Roland Kullmer, Reinhard Holecek, Christoph Lugmair, Matthias Krawinkler, Volker Strobl, Tribological behavior of thick DLC coatings under lubricated conditions, *Surf. Coat. Technol.* 314 (2017) 13–17.
- [25] N. Vidakis, A. Antoniadis, N. Bilalis, The VDI 3198 indentation test evaluation of a reliable qualitative control for layered compounds, *J. Mater. Proc. Technol.* 143–144 (2003) (2003) 481–485.
- [26] S. Gayathri, N. Kumar, R. Krishnan, T.R. Ravindran, S. Dash, A.K. Tyagi, M. Sridharan, Influence of Cr content on the micro-structural and tribological properties of PLD grown nanocomposite DLC-Cr thin films, *Mater. Chem. Phys.* 167 (2015) 194–200.
- [27] R.Y. Wang, L.L. Wang, H.D. Liu, S.J. Yan, Y.M. Chen, D.J. Fu, B. Yang, Synthesis and characterization of CrCN-DLC composite coatings by cathodic arc ion plating, *Nucl. Instrum. Methods Phys. Res. Sect. B* 307 (2013) 185–188.
- [28] W. Dai, G. Wu, A. Wang, Preparation, characterization and properties of Cr-incorporated DLC films on magnesium alloy, *Diam. Relat. Mater.* 19 (2010) 1307–1315.
- [29] V. Singh, J.C. Jiang, E.I. Meletis, Cr-diamond like carbon nanocomposite films: synthesis, characterization and properties, *Thin Solid Films* 489 (2005) 150–158.
- [30] Weierstraß-Institut für Angewandte Analysis und Stochastik, Preprint ISSN 0946–8633, No. 1306, Berlin, 2008, pp. 1–14.
- [31] Xudong Sui, Jinyu Liu, Shuaituo Zhang, Jun Yang, Junying Hao, Microstructure, mechanical and tribological characterization of CrN/DLC/Cr-DLC multilayer coating with improved adhesive wear resistance, *Appl. Surf. Sci.* 439 (2018) 24–32.
- [32] N.P. Barradas, C. Jaynes, R.P. Webb, U. Kreissig, R. Grötzschel, Unambiguous automatic evaluation of multiple ion beam analysis data with simulated annealing, *Nucl. Instrum. Methods Phys. Res. B* 149 (1999) 233.
- [33] N.P. Barradas, C. Pascual-Izarra, Double scattering in RBS analysis of PtSi thin films on Si, *Nucl. Instrum. Methods Phys. Res. B* 228 (2005) 378–382.
- [34] N.P. Barradas, M. Reis, Accurate calculation of pileup effects in PIXE spectra from first principles, *X-Ray Spectrom.* 35 (2006) 232–237.
- [35] W.C. Oliver, G.M. Pharr, An improved technique for determining hardness and elastic modulus using load and displacement sensing indentation experiments, *J. Mater. Res.* 47 (1992) 1564–1583.
- [36] H.P. Schulze, W. Schätzing, Influences of different contaminations on the electro-erosive and the electrochemical micro-machining, *Pro. CIRP* 6 (2013) 58–63.
- [37] N. Kumar, Neha Sharma, S. Dash, C. Popov, W. Kulisch, J.P. Reithmaier, G. Favaro, A.K. Tyagi, Baldev Raj, Tribological properties of ultrananocrystalline diamond films in various test atmosphere, *Tribol. Int.* 44 (2011) 2042–2049.
- [38] A. Lippitz, Th. Hubert, *Surf. Coat. Technol.* 200 (2005) 250–253.
- [39] O. Nishimura, K. Yabe, M. Iwaki, *J. Electron Spectrosc. Relat. Phenom.* 49 (1989) 335–342.
- [40] A.V. Naumkin, A. Kraut-Vass, S.W. Gaarenstroom, C.J. Powell, NIST X-ray photoelectron spectroscopy database, NIST Standard Reference Database 20, version 4.1 (2012).
- [41] A.C. Ferrari, J. Robertson, Interpretation of Raman spectra of disordered and amorphous carbon, *Phys. Rev. B* 61 (2000) 14095–14107.
- [42] C. Adelhelm, M. Balden, M. Rinke, M. Stueber, Influence of doping (Ti, V, Zr, W) and annealing on the sp² carbon structure of amorphous carbon films, *J. Appl. Phys.* 105 (2009) 033522-1–9.
- [43] Dariya Savchenko, Vladimir Vorlíček, Andrey Prokhorov, Ekaterina Kalabukhova, Jan Lančok, Miroslav Jelínek, Raman and EPR spectroscopic studies of chromium carbon films, *Diam. Relat. Mater.* 83 (2018) 30–37.
- [44] Luis Yate, Leyre Martínez-de-Olcoz, Joan Esteve, Arturo Lousa, Ultra low nanowear in novel chromium/amorphous chromium carbide nanocomposite films, *Appl. Surf. Sci.* 420 (2017) 707–713.